International Journal of Naval Architecture and Ocean Engineering 12 (2020) 569–577

Contents lists available at ScienceDirect

International Journal of Naval Architecture and Ocean Engineering

journal homepage: http://www.journals.elsevier.com/international-journal-of-naval-architecture-and-ocean-engineering/

Numerical and experimental study on the scale effect of internal solitary wave loads on spar platforms

Xu Wang [a,*], Ji-Fu Zhou [a,b]

[a] *Key Laboratory for Mechanics in Fluid Solid Coupling System, Institute of Mechanics, Chinese Academy of Sciences, Beijing, 100190, China*
[b] *School of Engineering Sciences, University of Chinese Academy of Sciences, Beijing, 100049, China*

ARTICLE INFO

Article history:
Received 14 April 2020
Received in revised form
24 May 2020
Accepted 3 June 2020
Available online 31 July 2020

Keywords:
Internal solitary wave loads
Spar platform
Scale effect

ABSTRACT

Based on laboratory experiments and numerical simulations, the scale effect of Internal Solitary Wave (ISW) loads on spar platforms is investigated. First, the waveforms, loads, and torques on the spar model at a laboratory obtained by the experiments and simulations agree well with each other. Then, a prototype spar platform is simulated numerically to elucidate the scale effect. The scale effect for the horizontal forces is significant owing to the viscosity effect, whereas it is insignificant and can be neglected for the vertical forces. From the similarity point of view, the Froude number was the same for the scaled model and its prototype, while the Reynolds number increased significantly. The results show that the Morison equation with the same set of drag and inertia coefficients is not applicable to estimate the ISW loads for both the prototype and laboratory scale model. The coefficients should be modified to account for the scale effect. In conclusion, the dimensionless vertical forces on experimental models can be applied to the prototype, but the dimensionless horizontal forces of the experimental model are larger than those of the prototype, which will lead to overestimation of the horizontal force of the prototype if direct conversion is implemented.

1. Introduction

A large number of observations show that Internal Solitary Waves (ISWs) occur frequently and exist widely in the ocean due to density stratification arising from salinity and temperature variations (Apel et al., 1985). ISWs can cause severe impacts on the operation of ocean engineering structures (Osborne and Burch, 1980), even causing a cable breakage as occurred in the extended test period of the Liuhua oilfield in the South China Sea (Bole et al., 1994). As a floating structure, the spar platform is well suited for deep-water applications such as drilling, production, processing, storage and off-loading of ocean deposits. In regions with frequent occurrence of ISWs, it is necessary to assess the hydrodynamic impacts of ISWs on spar platforms.

Laboratory experiments are a reliable approach to study hydrodynamic loads; however, the scale effect is an intrinsic issue that affects the conversion from laboratory results to the prototype. Owing to the size limit of laboratory tanks, the similarity relations (such as geometric relations, the Froude and Reynolds numbers) are difficult to meet simultaneously. Therefore, it is of great importance to elucidate whether dimensionless experimental loads can be applied to directly estimate the prototype loads. Taking ship resistance trials as an example, only the similarity relations of the Froude number and the geometry can be met, whereas the similarity of Reynolds number can be hardly assured (Van Manen et al., 1988). The traditional spar platform can be simplified as a cylinder structure. There is extensive research on the scale effect in studies of cylinder/spar platforms under the action of surface waves (Ran et al., 1996; Utsunomiya et al., 2013). However, there are only a few studies on the scale effect for ISW loads, so that the relation between the experimental model and its prototype is still unclear. Additionally, in engineering applications the Morison formula (Morison et al., 1950) has been widely used to calculate the ISW loads of a cylinder structure (Cai et al., 2008; Si et al., 2012; Song et al., 2011). Nonetheless, the inertial force and drag force coefficients in the Morison formula can be determined by referring to the calculation of the surface-wave loads (Sarpkaya, 2001, Sarpkaya, 2005). It is unclear if the coefficients can be applied to calculate the ISW loads for a structure of either laboratory scale or full-size prototype.

* Corresponding author.
E-mail address: wangxu@imech.ac.cn (X. Wang).
Peer review under responsibility of Society of Naval Architects of Korea.

https://doi.org/10.1016/j.ijnaoe.2020.06.001

Numerical simulation can directly obtain the hydrodynamic characteristics and load compositions. Thus, it provides a way to uncover the ISW load components and to analyze the scale effect of ISW loads on spar platforms. For the semi-submersible platform the components of the ISW loads are investigated (Wang et al., 2018), and results demonstrate that the numerical simulation method is accurate and effective.

In the present paper, the scale effect and similarity relations regarding ISW loads on spar platforms are analyzed and discussed. The paper is organized as follows. Following the introduction, Section 2 briefly describes the experimental facility and numerical implementation. Section 3 discusses the scale effect of ISW loads and the similarity relations. Finally, the conclusions are presented in Section 4.

2. Methodology

2.1. Experimental facility and procedure

The experiments were carried out in the large-scale density stratified tank (length: 30 m, width: 0.6 m, height: 1.2 m) at Shanghai Jiao Tong University (Fig. 1). Two steel plates are located at the front end of the tank for ISW generation, the experimental model and measuring equipment are arranged in the intermediate region, and a wedge-shape wave breaker is set up at the rear end of the tank to prevent the reflection of solitary waves.

The experimental model is shown in Fig. 2. The forces on the spar platform during the ISW propagation are measured by the three-component force balance, which is connected to the model and attached to the top of the tank. Before the experiment, an additional weight is introduced to ensure the balance between gravity and buoyancy of the model. Then, we load and unload weights on the model along the horizontal and vertical directions respectively in order to obtain the calibration relationship between the measured electronic signals and loads. During the experiment, the ISW loads on the model can be calculated from the electronic signals according to the calibration relationship.

The stratified two-layer fluid in the tank was prepared in the following way. First we injected the upper-layer fluid until its height was h_1, then slowly injected the lower-layer fluid from two mushroom-type inlets at the bottom of the tank until the total height was h. Thus the thickness of the lower-layer is $h_2 = h - h_1$.

In the experiment the ISWs were generated using a double-plate wave maker (black plates in Fig. 1), unlike the system used in the gravity collapse method (Du et al., 2016). The procedure is similar to that described by Wessels and Hutter (1996). Two improvements were applied to generate nonlinear ISWs with higher amplitudes. First, the drive mechanism of the wave-maker was significantly upgraded and the control software of the two plates was modified. Then, a steel plate, with size adjusted through tests, was placed on top of the wave-maker to reduce the disturbance of the free surface.

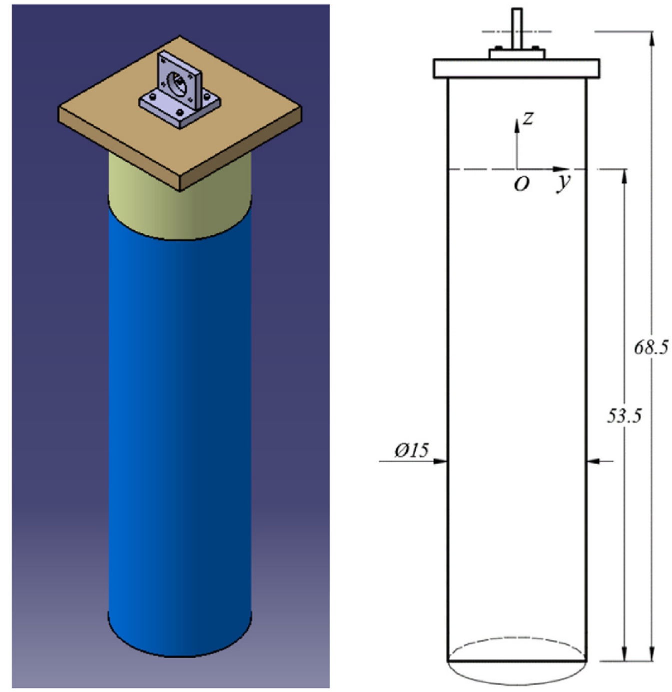

Fig. 2. The experimental model (left) and a sketch of the front of the model with dimensions (right) (unit: cm).

The two steel plates move along in opposite directions at different speeds to generate an ISW at the interface between the two layers. At the preparation stage, the two plates were set to the same heights as the undisturbed fluid layers (h_1, h_2). During the generation process, the speed of the upper and lower plates ($\overline{u}_1$, $\overline{u}_2$), respectively, was controlled by a computer and can be expressed as:

$$\overline{u}_1 = -c \cdot \zeta(t)/h_1,\ \overline{u}_2 = c \cdot \zeta(t)/h_2, \tag{1}$$

where c is the phase speed, and $\zeta(t)$ denotes the interface displacement of the desired ISW.

The ISWs were measured using two rows of conductivity probes which were arranged at 3-m intervals. Each row comprised 13 equally distributed probes, and the distance between the rows was 3 cm. It is known that the conductivity has a linear relationship with the density variation, so we can easily obtain the ISW interface displacement as well as the phase speed by post-processing the conductivity signal measured by the two rows of probes.

The trailing-wave phenomenon behind the leading ISW is often unavoidable in the experiment stage. The existence of the trailing waves implies the dissipation of wave energy during wave generation. As a result, the measured amplitude is always less than the

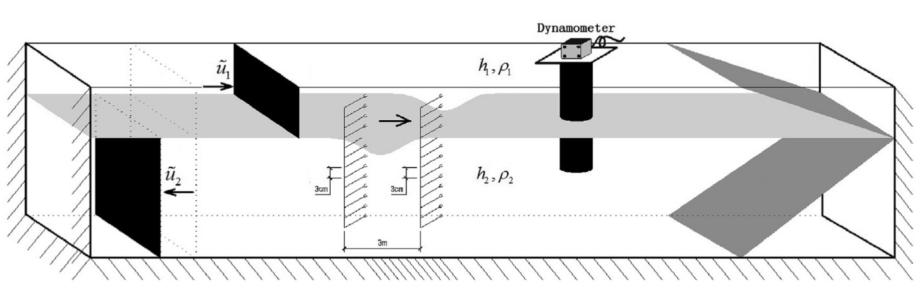

Fig. 1. Illustration of internal solitary wave generation by a double-plate wave-maker.

desired amplitude for the experiment. To generate the desired waveform for a specific case, first we have to find the relation between the measured amplitude a_m and the desired amplitude a_d based on a series of experiments. Then the desired amplitude can be achieved by adjusting the input parameters according to the relation mentioned above.

2.2. Numerical methods and implementation

Under the two-layer fluid approximation, a numerical model of a flume (Fig. 3) was built to simulate the nonlinear interactions between ISWs and a spar platform, where the ISWs were obtained by adding a mass source/sink term to the continuity equation. For an incompressible fluid of density ρ_i, the governing equations can be written as:

$$\mathrm{u}_{ix} + \mathrm{v}_{iy} + \mathrm{w}_{iz} = \begin{cases} 0, & (x,y,z) \notin \Omega \\ S_i(x,y,z,t)/\rho_i, & (x,y,z) \in \Omega \end{cases}, \tag{2}$$

$$\mathrm{u}_{it} + u_i \mathrm{u}_{ix} + v_i \mathrm{u}_{iy} + w_i \mathrm{u}_{iz} = -p_{ix}/\rho_i + \nu(\mathrm{u}_{ixx} + \mathrm{u}_{iyy} + \mathrm{u}_{izz}), \tag{3}$$

$$\mathrm{v}_{it} + u_i \mathrm{v}_{ix} + v_i \mathrm{v}_{iy} + w_i \mathrm{v}_{iz} = -p_{iy}\Big/\rho_i + \nu(\mathrm{v}_{ixx} + \mathrm{v}_{iyy} + \mathrm{v}_{izz}), \tag{4}$$

$$\mathrm{w}_{it} + u_i \mathrm{w}_{ix} + v_i \mathrm{w}_{iy} + w_i \mathrm{w}_{iz} = -p_{iz}/\rho_i + \nu(\mathrm{w}_{ixx} + \mathrm{w}_{iyy} + \mathrm{w}_{izz}) - g, \tag{5}$$

where (u_i, v_i, w_i) are the velocity components (u_i, v_i, w_i) in Cartesian coordinates and P_i is the pressure. Note that the subscripts with respect to space and time represent partial differentiation, and *i*=*1* (*i*=*2*) denotes the upper (lower) layer fluid. g is the gravitational acceleration.

The additional mass source term $S_i(x,y,z,t)$ in Eq. (1) is a nonzero function only in the source region Ω.

Bordered by the ISW interface, the source region can be divided into two subregions: Ω_1 and Ω_2, which denote the source region and the sink region, respectively. The source/sink term $S_i(t)$ is given by (Wang et al., 2017):

$$S_1(t) = -\rho_1 c \frac{\zeta(t)}{h_1 - \zeta(t)} \frac{1}{\Delta x}, \quad S_2(t) = \rho_2 c \frac{\zeta(t)}{h_2 + \zeta(t)} \frac{1}{\Delta x}. \tag{6}$$

where c denotes the phase speed, Δx is the width of the mass source region, and $\zeta(t)$ is the interface displacement of the ISW.

The Volume Of Fluid (VOF) method (Hirt and Nichols, 1981) was employed to track the ISW interface $z = \zeta(x,y,t)$.

At the interface, the normal velocity is continuous, and so is the pressure. For the top and bottom of the fluid domain we used the rigid-lid approximation and the surface of the platform was set as an impermeability boundary. The forces and torque on the surface were monitored during the simulation. Moreover, a symmetry condition was imposed on the left boundary in the source term wave-generation method. The right boundary was set as a smooth non-slip wall. To prevent wave reflection at the end of the domain, a buffering region was allocated to dissipate the ISWs in the numerical flume, which was realized by adding a source term to the momentum equation in the vertical direction.

The initial condition is still water with no wave or current motion.

The numerical model works as follows: first the ISW interface displacement $\zeta(t)$ is calculated, then $\zeta(t)$ is placed in the mass source function given by Eq. (6), and finally the ISW is excited in the source term region. During the propagation of the ISW, the forces on the spar platform are monitored in real time. It should be noted that although the numerical simulation is carried out with User Defined Function (UDF) redevelopment tools on the platform of the Fluent software, it is still applicable to other calculation platforms.

The governing equations were discretized on three-dimension structured grids using a Finite Volume Method (FVM) and well-chosen numerical schemes were selected to avoid spurious effects. In addition, structured elements were used to ensure the mesh quality of the computational domain. Particularly, local grid refinements were employed to reduce the numerical dispersion near the interface and spar platform (shown in Fig. 4), while sparse grids were employed to reduce the computational burden in the buffering region.

2.3. Forces on the spar platform

The horizontal force F_x, vertical force F_z and torque M_y were measured by the three-component force balance at the experiment stage and monitored during the simulation. The lateral force F_y (caused by a periodic trailing vortex behind the spar platform) is much weaker than F_x or F_z, so it is not discussed in the paper. F_x and F_z on a spar platform can be expressed as:

$$F_x = \mu \int_S \left(\left(\frac{\partial u}{\partial y} + \frac{\partial v}{\partial x} \right) n_y + \left(\frac{\partial u}{\partial z} + \frac{\partial w}{\partial x} \right) n_z \right) ds + \int_S - p n_x ds, \tag{7}$$

$$F_z = \mu \int_S \left(\left(\frac{\partial u}{\partial z} + \frac{\partial w}{\partial x} \right) n_x + \left(\frac{\partial v}{\partial z} + \frac{\partial w}{\partial y} \right) n_y \right) ds + \int_S - p n_z ds, \tag{8}$$

where μ denotes the dynamic viscosity of water $(1.01 \times 10^{-3}\ N \cdot s/m^2)$, S is the wetted surface of the spar platform, and $(n_x\ n_y,\ n_z)$ is the outward unit normal vector of the surface. For formulas (12), (13), the forces consist of two parts, where the first term represents the friction $(f_x f_z)$ and the second one represents the pressure-difference force $(F_x^p,\ F_z^p)$.

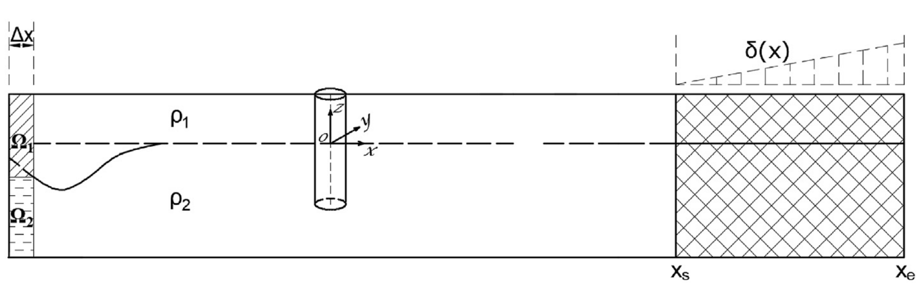

Fig. 3. Front view of the 3D computation domain.

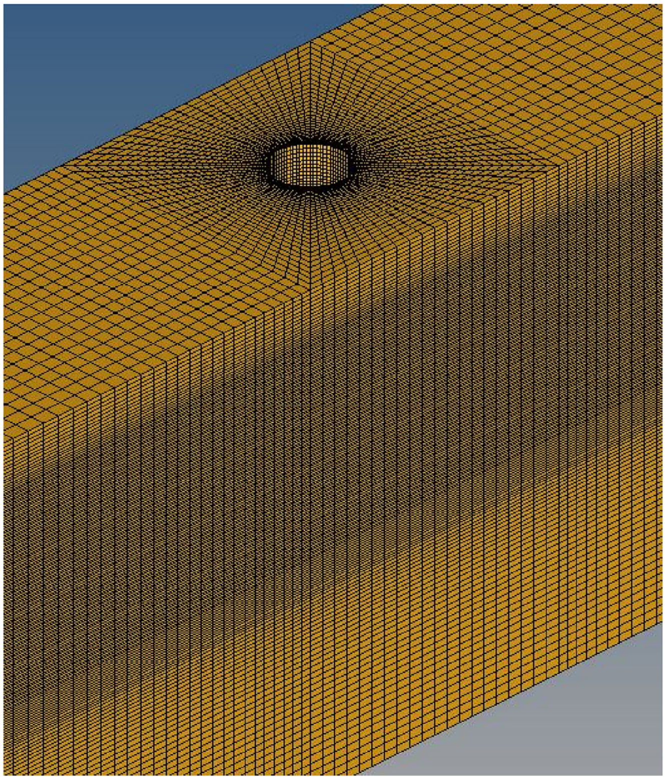

Fig. 4. The grid distribution near the spar platform.

$$F_x^p = \int_s -pn_x ds, \tag{9}$$

$$F_z^p = \int_z -pn_z ds, \tag{10}$$

$$f_x = \mu \int_s \left(\left(\frac{\partial u}{\partial y} + \frac{\partial v}{\partial x} \right) n_y + \left(\frac{\partial u}{\partial z} + \frac{\partial w}{\partial x} \right) n_z \right) ds, \tag{11}$$

$$f_z = \mu \int_s \left(\left(\frac{\partial u}{\partial z} + \frac{\partial w}{\partial x} \right) n_x + \left(\frac{\partial v}{\partial z} + \frac{\partial w}{\partial y} \right) n_y \right) ds. \tag{12}$$

Furthermore, to study constituents of the load, according to the contribution of the viscosity, the pressure-difference force can be divided into two components: wave pressure-difference force (F_x^{pw} F_z^{pw}) and viscous pressure-difference force (F_x^{pv} F_z^{pv}). The wave pressure-difference force is associated with the fluctuation of water parcels, which can be calculated based on the Euler equations, while the viscous pressure-difference force is associated with the viscous effect, which can be calculated by subtracting the wave pressure-difference force obtained by the Euler equations from the one obtained by the Navier-Stokes (N–S) equations. The expressions of (F_x^{pw} F_z^{pw}) and (F_x^{pv} F_z^{pv}) are given as:

$$F_x^{pw} = \int_s -pn_x ds_{\ (\mathrm{Euler})}, \tag{13}$$

$$F_z^{pw} = \int_s -pn_z ds_{\ (\mathrm{Euler})}, \tag{14}$$

$$F_x^{pv} = \int_s -pn_x ds_{\ (\mathrm{N-S})} - \int_s -pn_x ds_{\ (\mathrm{Euler})}, \tag{15}$$

$$F_z^{pv} = \int_s -pn_z ds_{\ (\mathrm{N-S})} - \int_s -pn_z ds_{\ (\mathrm{Euler})}. \tag{16}$$

To facilitate the comparison with experiment measurements, the moment center is placed at the joint point of the experiment model and the three-component force balance (see Fig. 2(a)). Considering the symmetry of the model and neglecting the slightly nonuniform distribution of the vertical force over the horizontal wetted surfaces of the structure, we have the torque M_y given by

$$M_y = \mu \int_s \left(\left(\frac{\partial u}{\partial y} + \frac{\partial v}{\partial x} \right) n_y + \left(\frac{\partial u}{\partial z} + \frac{\partial w}{\partial x} \right) n_z \right) \cdot \overline{d} \cdot ds + \int_s -pn_x \cdot \overline{d} \cdot ds, \tag{17}$$

where $\overline{d}$ is the arm of the horizontal force of each wetted cell of the structure, namely the vertical distance between the cell center and the moment center.

3. Results and discussion

In this section, we discuss the scale effects for the ISW loads on spar platforms, comparing the experimental model with its prototype. The scaled model was constructed at a ratio of $k = 200:1$ relative to a real-size spar platform. The parameters for the flume and model at different scales are listed in Table 1.

3.1. Validation of numerical model

Fig. 5 shows the wave profiles of the ISWs of the Computational Fluid Dynamics (CFD) simulations, ISW theory (eKdV) and laboratory experiments for Case A. Both the numerical and experimental waveforms are in good agreement with the theoretical results (the relative errors are within 3%), which indicates that the experimental wave-maker and numerical approaches can accurately

Table 1
The parameters for the flume and model at different scales.

ID	k	Length (m)	Width (m)	Height (m)	Diameter (m)	draft (m)	ρ_1 ($kg \cdot m^{-3}$)	ρ_2 ($kg \cdot m^{-3}$)
Case A	1:1	30	0.6	1	0.15	0.535	998	1025
Case B	200:1	6000	120	200	30.0	107.00	998	1025

ID	k	h_1 (m)	h_2 (m)	a (m)	Grid quantity	Time step (s)
Case A	1:1	0.3	0.7	0.101	1,824,952	0.005
Case B	200:1	60	140	20.2	4,201,860	0.07

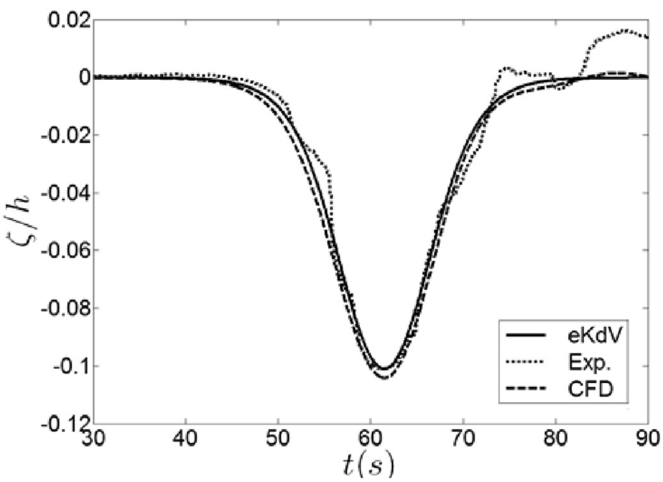

Fig. 5. Comparisons of profiles of ISWs between CFD simulations (dotted curve), ISW theory (solid curve), and laboratory experiments (dash-dotted curve) for Case A.

generate the waveform in the presence of platforms.

Here, we define $\overline{F}_x = F_x/(\rho_1 g\nabla)$, $\overline{F}_z = F_z/(\rho_1 g\nabla)$ and $\overline{M}_y = M_y/(\rho_1 gd\nabla)$ as the dimensionless ISW-generated horizontal and vertical forces, and the torque, respectively, on the spar platform. Fig. 6 shows the time variations of the dimensionless loads and torque for Case A. The numerical and experimental results are in good agreement, indicating that it is reasonable and feasible to calculate the loads and torque on the spar platform based on the proposed numerical flume. According to Eq. (17), the torque $\overline{M}_y$ is proportional to the horizontal load $\overline{F}_x$. Hence, we primarily focus on $\overline{F}_x$ and $\overline{F}_z$ in the subsequent analysis.

In order to verify the grid and time step independence, 2 different grid distribution cases and 2 different time step cases are performed with Case A. The simulated maximum loads ($\overline{F}_x^{max}$, $\overline{F}_z^{max}$) and corresponding errors relative to experimental results are listed in Tables 2 and 3. It is seen that more refined grid and smaller time step than originally used do not improve the precision significantly. It indicates that numerical results with such grid distribution and time step are stable and convergent for Case A. In the same way, numerical test examples also demonstrate the numerical convergence with the grid and time step employed in Case B (the prototype scale).

3.2. The scale effect of the total ISW loads

For ease of discussion, we define $\bar{t} = t/\sqrt{k}$ as the scaled time; the

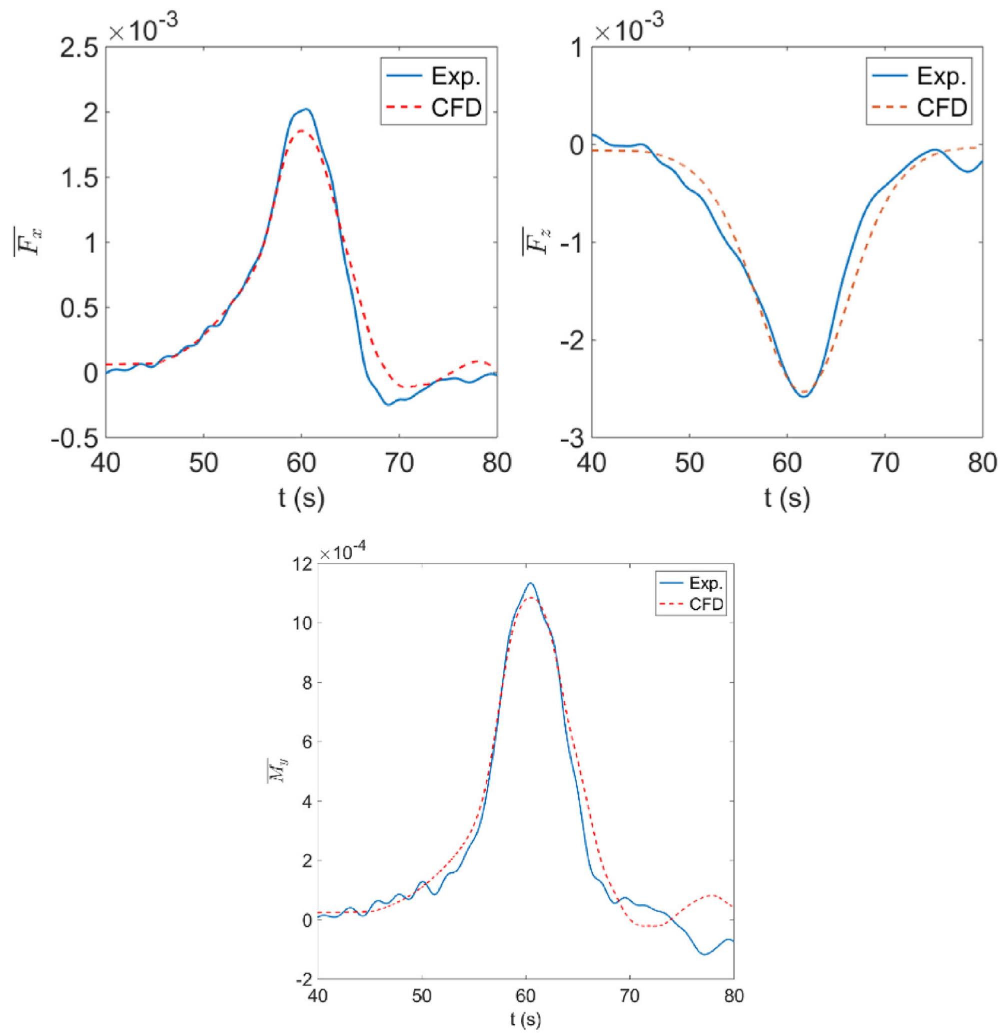

Fig. 6. Experimental and numerical time variation of the ISW-generated dimensionless loads and torque for Case A.

Table 2
The numerical results for the grid-independence test (iteration step: 0.005s).

ID	Grid quantity	$\overline{F}_x^{max}$ (%)	$\overline{F}_z^{max}$ (%)
Case A	1,824,952	1.90e-3 (5.06%)	2.50e-3(3.84%)
Case A-GridTest1	2,134,794	1.90e-3 (5.06%)	2.51e-3 (3.46%)
Case A-GridTest2	2,365,738	1.90e-3 (5.06%)	2.51e-3 (3.46%)

Table 3
The numerical results for the time step-independence test (grid quantity: 1,824,952).

ID	Time step	$\overline{F}_x^{max}$ (%)	$\overline{F}_z^{max}$ (%)
Case A	0.005	1.90e-3 (5.00%)	2.50e-3(3.84%)
Case A-TimeStepTest1	0.004	1.90e-3 (5.00%)	2.50e-3(3.84%)
Case A-TimeStepTest2	0.003	1.90e-3 (5.00%)	2.50e-3(3.84%)

dimensionless horizontal $\overline{F}_x$ and vertical forces $\overline{F}_z$ are defined as described in Section 3.1.

As shown in Fig. 7, both horizontal and vertical forces follow a similar trend, almost simultaneously peaking at $\bar{t} = 61$. However, the relative error of the maximum amplitude for the horizontal force is 25.66% between the model and the prototype, while it is only 8.17% for the vertical forces. This indicates that the scale effect is highly significant for the horizontal forces and limited for the vertical forces. Next, the causes of these differences will be discussed from the point of view of the load components.

To discuss the components of the ISW loads, it is necessary to analyze the influence of fluid viscosity on the generation and propagation of ISWs. We carried out two simulations based on the Navier-Stokes equations and the Euler equations. The wave profiles for Case A simulated by the two systems are shown in Fig. 8. The results show that the waveforms generated by the two simulation approaches remain stable with only slight differences between the two profiles, which indicates that the influence of fluid viscosity on the ISW propagation is limited.

3.2.1. The scale effect of the horizontal loads

For the horizontal force, the time variations of the wave and viscous pressure-difference forces, as well as the friction are shown in Fig. 9. Comparing Fig. 9(a) and (b), the friction is always small and can be considered negligible. The changes in the wave pressure-difference forces from Case A to Case B and not great (the relative error of the amplitude is about 20%, shown in Fig. 10). However, the viscous pressure-difference forces change significantly (relative error of 38%). This indicates that the scale effect is influenced mainly by the viscosity characteristics.

3.2.2. The scale effect of the vertical loads

The time variations of the wave and viscous pressure-difference forces, and the friction for the vertical force are shown in Fig. 11. For Case A and Case B, the friction is negligible and portions of the viscous pressure-difference forces are quite small, while the wave pressure-difference forces are the dominant component (see Fig. 12). These results indicate that the influence of the viscosity on the scale effect is minimal.

3.3. Analysis of similarity relations

The results shown above can be explained by the similarity theory. With regard to the spar platform, the geometric similarity, Froude number (Fr) and Reynolds number (Re) should be taken into consideration. For simplicity, we can assume that the geometric scale ratio C_L is k. The theoretical analysis of the similarity criteria is presented below.

Depending on the parameters of the set-up, solitary waves can be either of elevation or depression, moving with speed c related to its (signed) amplitude a (Camassa et al., 2006):

$$\frac{c^2}{c_0^2} = \frac{(h_1 - a)(h_2 + a)}{h_1 h_2 - (c_0^2/g)a}, \tag{18}$$

where c_0 is the linear long wave speed defined by

$$c_0^2 = g\frac{h_1 h_2(\rho_2 - \rho_1)}{\rho_1 h_2 + \rho_2 h_1}, \tag{19}$$

For travelling-wave solutions of a strongly nonlinear system with speed c, the average velocity and the layer thickness are related by the exact expression

$$U_1 = c_0\frac{-\zeta}{h_1 - \zeta}\ ,\ \ U_2 = c_0\frac{\zeta}{h_2 + \zeta} \tag{20}$$

Hence, the velocity scale is $C_{U_i} = C_c = C_{c_0} = \sqrt{k}$ for both the upper and lower fluid layers. According to the definition of the Fr ($F_r = U_i/\sqrt{gL}$) and R_e ($R_e = LU_i/\nu$), their scale relations are $C_{F_r} = 1$,

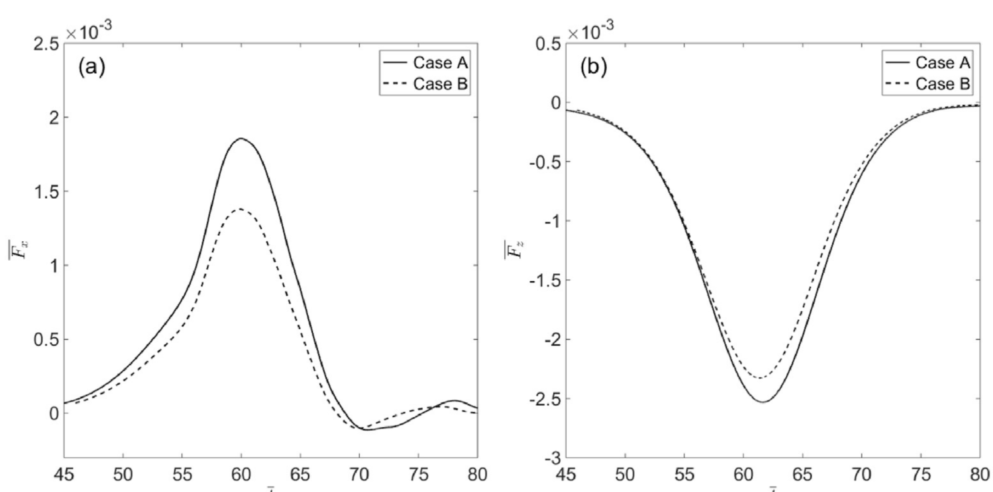

Fig. 7. Comparisons of (a) horizontal forces and (b) vertical forces at different scales.

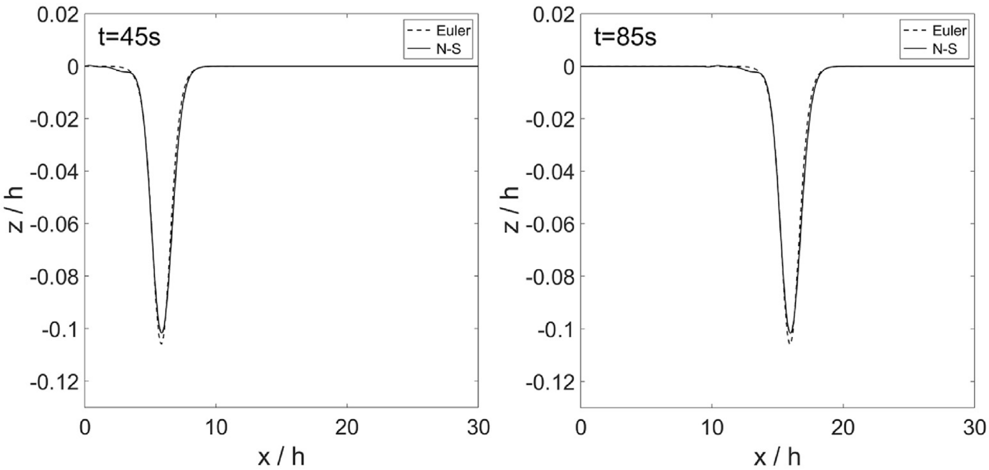

Fig. 8. The numerical results for the ISW waveforms using Euler and Navier-Stokes based simulations for Case A.

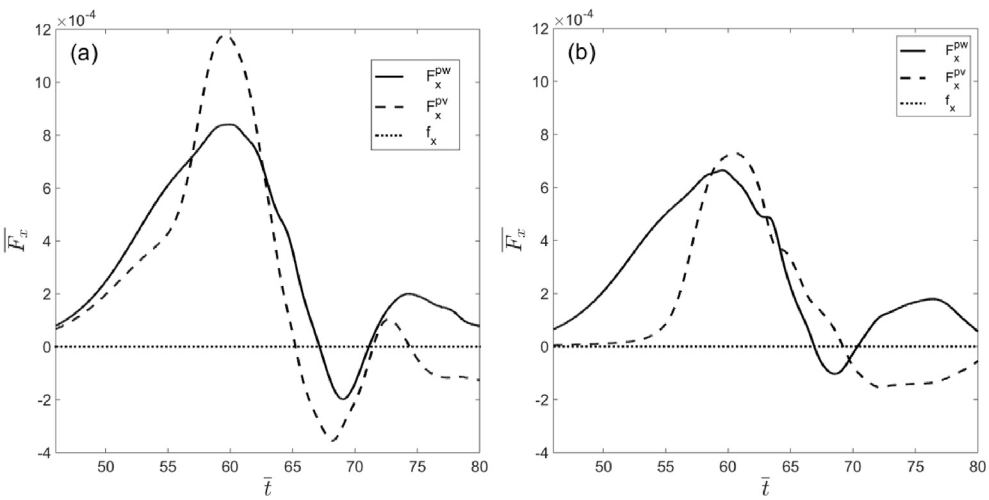

Fig. 9. Horizontal force components for different scale models; (a) Case A, (b) Case B.

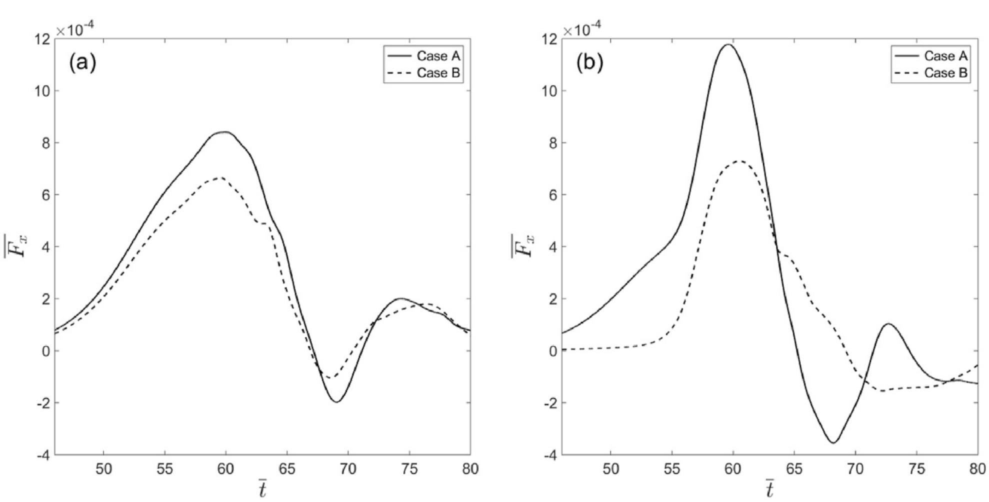

Fig. 10. (a) Wave pressure-difference force curves and (b) viscous pressure-difference force curves for horizontal loads for the experimental model and its prototype.

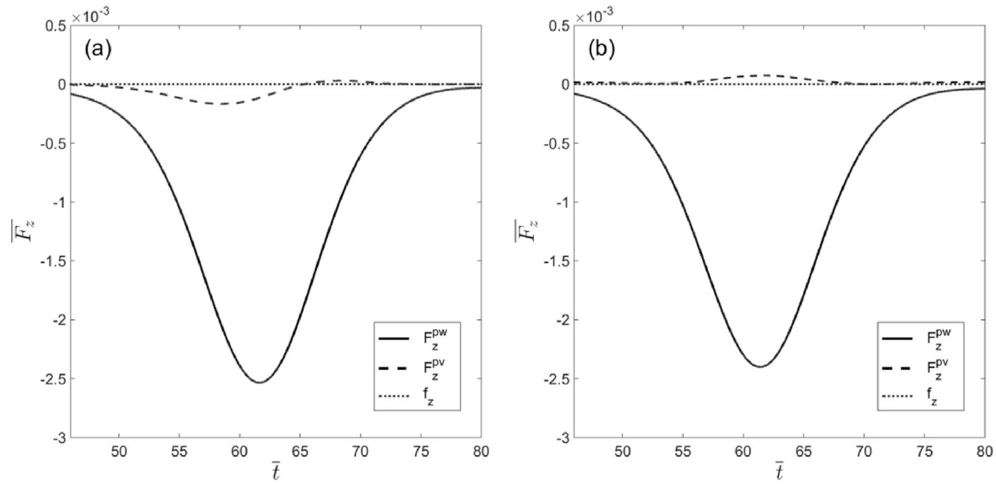

Fig. 11. The components of the vertical forces for the different scale models. (a) Case A, (b) Case B.

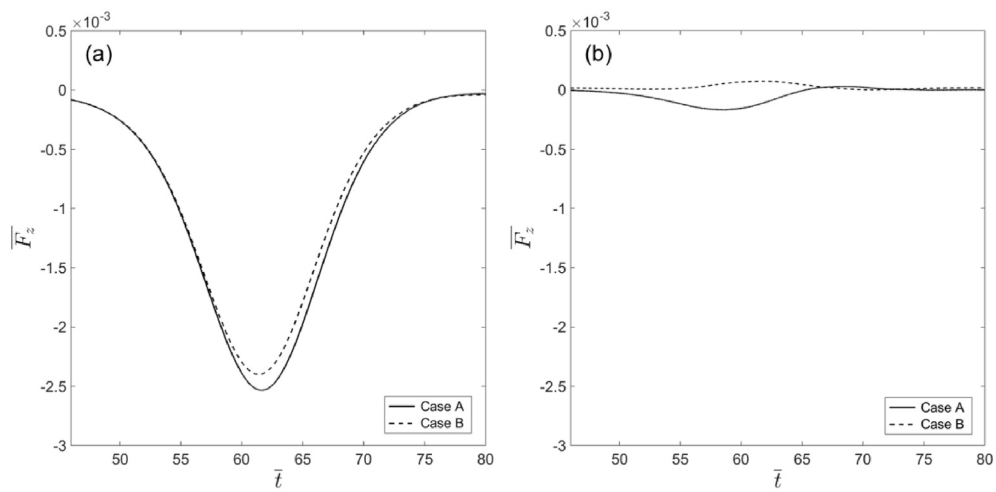

Fig. 12. (a) Wave pressure-difference force curve and (b) viscous pressure-difference force curve for vertical loads the experimental model and its prototype.

and $C_{R_e} = \sqrt{k}$. In addition, the scale relation C_t of time t ($t = L/c$) can be written as $\sqrt{k}$ (That is why we define $\bar{t} = t/\sqrt{k}$ in Section 3.1).

Overall, the similarity criteria between the spar platform model and its prototype are summarized in Table 4.

Generally, the Reynolds and Froude numbers represent the actions of the viscosity and free surface. In Table 4 the Reynolds number increases significantly from the scaled model to the actual size, while the Froude number remains the same. This relationship implies significant differences between the viscosity actions of the model and the prototype that lead to a strong influence on the scale effect of the horizontal forces, as shown in Section 3.2. For the vertical force, the scale effect is very small due to the low influence of the viscosity, which agrees with the conclusions in Section 3.2.

The Morison equation is an empirical formula that is widely used to calculate the ISW loads of a cylinder structure. With the average velocity (Eq. (20)) in a two-layer fluid, it can be written as:

$$F_{\mathrm{Mor}} = \int C_D \rho_i \frac{D}{2} U_i |U_i| dz + \int C_M \rho_i \frac{\pi D^2}{4} \frac{\partial U_i}{\partial t} dz, \tag{21}$$

where C_D and C_M are the drag and inertia coefficients, respectively.

The similarity relation for dimensionless $\overline{F}_{Mor}$ $\left(\overline{F}_{Mor} = \frac{F_{\mathrm{Mor}}}{\rho_1 g \nabla}\right)$ can be derived from Eq. (21) as follows.

$$C_{\overline{F}_{Mor}} = \frac{C_D^{Actual} \cdot f_D + C_M^{Actual} \cdot f_M}{C_D^{Exp} \cdot f_D + C_M^{Exp} \cdot f_M}, \tag{22}$$

where $f_D = \int \rho_i \frac{D}{2} U_i |U_i| dz$ and $f_M = \int \rho_i \frac{\pi D^2}{4} \frac{\partial U_i}{\partial t} dz$ at the experimental

Table 4
The similarity criteria between the spar platform model and its prototype.

	geometry (L)	velocity (U_i)	R_e ($R_e = LU_i/\nu$)	F_r ($F_r = U_i/\sqrt{gL}$)
Similarity scale ratio	k	$\sqrt{k}$	$\sqrt{k}$	1

scale.

From Eq. (22), if the C_D and C_M remain the same ($C_D^{Actual} = C_D^{Exp}$, $C_M^{Actual} = C_M^{Exp}$) between the model and the prototype, $C_{\overline{F}_{Mor}}$ equals 1, which means the dimensionless force is invariant using the same set of coefficients in the Morison equation. However, this assumption is not valid (see the second paragraph in Section 3.1). Consequently, the Morison equation with the same set of coefficients is not applicable to estimate the ISW loads for both the model and the prototype. Therefore, the drag and inertia coefficients should be modified to account for the scale effect.

4. Conclusions

Numerical simulations and experiments were carried out to study the scale effect of internal solitary wave loads on spar platforms. The conclusions are summarized as follows:

(1) For the horizontal force, the scale effect on the viscous pressure-difference force is significant while the scale effect on the wave pressure-difference force is not obvious. For the vertical force, the scale effect can be neglected for both the wave and viscous pressure-difference forces. From the similarity point of view, the Froude number is the same for the laboratory scale model and its prototype, but the Reynolds number does not meet the similarity criteria. Therefore, the Morison equation with a same set of inertia and drag coefficients is not applicable to estimate the ISW loads for both the prototype and experimental model. The coefficients should be modified to account for the scale effect.

(2) It is feasible to take the dimensionless vertical forces measured in the laboratory as the dimensionless vertical loads on the prototype. However, the dimensionless horizontal force measured in the laboratory will overestimate the horizontal force of the prototype if the conversion is implemented directly.

Acknowledgments

We acknowledge the financial support of the National Key R&D Program of China (2017YFC1404202), the National Natural Science Foundation of China (11602274, and 11572332), and the Strategic Priority Research Program of the Chinese Academy of Sciences (XDB22040203, XDA22040304).

References

Apel, J.R., Holbrook, J.R., Liu, A.K., Tsai, J.J., 1985. The sulu sea internal soliton experiment. J. Phys. Oceanogr. 15 (12), 1625–1651.

Bole, J.B., Ebbesmeyer, C.C., Romea, R.D., 1994. Soliton currents in the south China sea:measurements and theoretical modeling. In: Offshore Technology Conference,Houston, USA, pp. 304–307.

Cai, S., Long, X., Wang, S., 2008. Forces and torques exerted by internal solitons in shear flows on cylindrical piles. Appl. Ocean Res. 30 (1), 72–77.

Camassa, R., Choi, W., Michallet, H., Rusås, P.-O., Sveen, J., 2006. On the realm of validity of strongly nonlinear asymptotic approximations for internal waves. J. Fluid Mech. 549, 1–23.

Du, H., Wei, G., Gu, M., Wang, X., Xu, J., 2016. Experimental investigation of the load exerted by nonstationary internal solitary waves on a submerged slender body over a slope. Appl. Ocean Res. 59, 216–223.

Hirt, C.W., Nichols, B.D., 1981. Volume of fluid (VOF) method for the dynamics of free boundaries. J. Comput. Phys. 39 (1), 201–225.

Van Manen, J.D., Van Ossanen, P., Lewis, E.V., 1988. Principles of Naval Architecture, Second Revision, Volume II: Resistance, Propulsion, and Vibration. Society of Naval Architects and Marine Engineers, Jersey City, New Jersey USA.

Morison, J.R., Johnson, J.W., Schaaf, S.A., 1950. The force exerted by surface waves on piles. J. Petrol. Technol. 2 (5), 149–154.

Osborne, A.R., Burch, T.L., 1980. Internal solitons in the andaman sea. Science 208 (4443), 451–460.

Ran, Z., Kim, M., Niedzwecki, J., Johnson, R., 1996. Responses of a spar platform in random waves and currents (experiment vs. theory). Int. J. Offshore Polar Eng. 6 (1).

Sarpkaya, T., 2001. On the force decompositions of Lighthill and Morison. J. Fluid Struct. 15 (2), 227–233.

Sarpkaya, T., 2005. On the parameter β=re/kc=d2/νt. J. Fluid Struct. 21 (4), 435–440.

Si, Z., Zhang, Y., Fan, Z., 2012. A numerical simulation of shear forces and torques exerted by large-amplitude internal solitary waves on a rigid pile in South China Sea. Appl. Ocean Res. 37 (37), 127–132.

Song, Z.J., Teng, B., Gou, Y., Lu, L., Shi, Z.M., Xiao, Y., Qu, Y., 2011. Comparisons of internal solitary wave and surface wave actions on marine structures and their responses. Appl. Ocean Res. 33 (2), 120–129.

Utsunomiya, T., Matsukuma, H., Minoura, S., Ko, K., Hamamura, H., Kobayashi, O., Sato, I., Nomoto, Y., Yasui, K., 2013. At sea experiment of a hybrid spar for floating offshore wind turbine using 1/10-scale model. J. Offshore Mech. Arctic Eng. 135 (3), 034503.

Wang, X., Zhou, J.F., You, Y.X., 2017. A numerical wave-maker for internal solitary waves with timely updated mass source/sink terms. Eur. J. Mech. B Fluid 65, 274–283.

Wang, X., Zhou, J.F., Wang, Z., You, Y.X., 2018. A numerical and experimental study of internal solitary wave loads on semi-submersible platforms. Ocean. Eng. 150, 298–308.

Wessels, F., Hutter, K., 1996. Interaction of internal waves with a topographic sill in a two-layered fluid. J. Phys. Oceanogr. 26 (1), 5–20.